Nanoscale Advances

ROYAL SOCIETY OF CHEMISTRY

PAPER

View Article Online
View Journal | View Issue

Cite this: *Nanoscale Adv.*, 2023, **5**, 4447

Preparation of cellulose nanocrystal (CNCs) reinforced polylactic acid (PLA) bionanocomposites filaments using biobased additives for 3D printing applications†

Victor Chike Agbakoba, *[ab] Percy Hlangothi,[b] Jerome Andrew[c] and Maya Jacob John[ab]

This work presents the experimental steps taken towards the preparation of 3D printable bionanocomposites using polylactic acid (PLA) biopolymer containing 0.1, 0.5 and 1 wt% CNCs. Optimized amounts of bio-based additives were added to improve the processability and flexibility of the bionanocomposites. The 3D printable bionanocomposite filaments were drawn using a single screw extruder. The bionanocomposites filament was used to 3D print prototypes and test specimens for dynamic mechanical analysis (DMA). Characterization of the CNCs and bionanocomposites was performed using Fourier Transform Infrared Spectroscopy (FTIR) analysis, differential scanning calorimetry (DSC) and thermogravimetric analysis (TGA). The nucleating effect of CNCs enhanced the crystallization behaviour of bionanocomposites by 5%, 15% and 11%, for the different CNCs loadings. The TGA analysis revealed a ~20 °C improvement in the thermal stability of the bionanocomposites. Meanwhile, the tensile analysis showed a ≥48% increase in the tensile strength of the bionanocomposites filaments which was attributed to the reinforcing effects of CNC. The addition of CNCs significantly increased the melt viscosity, storage and loss modulus of PLA. In summary, the bionanocomposite filaments produced in this study exhibited excellent processibility and superior mechanical and thermal properties.

Received 28th April 2023
Accepted 27th July 2023

DOI: 10.1039/d3na00281k

rsc.li/nanoscale-advances

1. Introduction

The fused deposition modelling (FDM) 3D printing technique is a material extrusion (MEX)-based technique that operates *via* a layer-by-layer melt deposition of thermoplastics following a pre-determined digitally generated build-path.[1] Presently, polylactic acid (PLA) remains the most widely used biopolymer in 3D printing due to its low melting point, minimal thermal shrinkage and warping.[2] However, the overall performance of pristine PLA is limited by its brittle nature, slow crystallization, and poor melt strength.[2,3] Strategies adopted towards improving the properties of PLA includes the incorporation of nano-reinforcements,[4,5] the use of biobased plasticizers[5,6] and blending with other biopolymers.[7–9] The development of eco-friendly 3D printable biopolymer-based composites has gained much attention in recent times. This is due to the drive for widespread adoption of eco-friendly, and biobased alternative material. Bionanocomposites of polylactic acid (PLA) biopolymer and nano cellulose possess promising physical and mechanical qualities desirable for FDM 3D printing applications. Attributes such as biocompatibility, potential biodegradability and wide-ranging applications make them an ideal material for a circular bioeconomy.[10]

Cellulose nanocrystals (CNCs) are rigid rod-shaped crystalline nanomaterials with diameters ranging from 1–100 nm and lengths between 50 to 1160 nm.[11–13] The interest in CNCs is due to their high aspect ratio, low density, renewability, biocompatibility, and biodegradability. CNCs are typically isolated from the crystalline domains of naturally occurring cellulosic sources like plant lignocellulosic biomass,[1–6] sea animal (tunicate)[14] and bacterial cellulose.[15] Presently sulphuric acid hydrolysis of cellulosic fibres is the most widely used CNC extraction method.[16,17] The introduction of unmodified CNCs into the PLA matrix has been shown to result in the lowering of tensile strength.[18] This is largely due to the tendency of CNCs to agglomerate inside the PLA matrix, which leads to poor interfacial interactions and low-stress transfer.[19,20] However, some studies have successfully demonstrated the use of CNCs to

[a]*Centre for Nanostructures and Advanced Materials, Council for Scientific and Industrial Research (CSIR), Chemicals Cluster, Pretoria, South Africa. E-mail: s215161440@mandela.ac.za*

[b]*Department of Chemistry, Nelson Mandela University, Port Elizabeth, South Africa*

[c]*Biorefinery Industry Development Facility, Council for Scientific and Industrial Research (CSIR), Durban, South Africa*

† Electronic supplementary information (ESI) available. See DOI: https://doi.org/10.1039/d3na00281k

improve the mechanical properties and crystallization behaviour of PLA filaments.[21–23] A recent study reported improved crystallinity and an 18% increase in the tensile strength of PLA after incorporating 1% CNCs powder.[24] The flexibility and processibility of bionanocomposites have been improved by the addition of bio-based plasticizers.[25,26]

The major challenges faced during the production of bionanocomposites are poor dispersion of nanomaterials in the polymer matrix, potential thermal degradation, poor compatibility and weak interfacial interactions.[25] Modification strategies such as surface functionalization of CNCs (*via* esterification, silylation and acetylation reactions), grafting, and the addition of coupling agents, compatibilizers and surfactants have been adopted to mitigate this problem.[18,27,28] Presently, direct liquid feeding and dry mixing process have been explored as viable strategies for producing CNC/PLA bionanocomposites. Typically, CNCs are dispersed in water, making them suitable for direct liquid feeding methods. However, this is undesirable as the water can initiate thermo-hydrolytic degradation of PLA during melt-mixing. To mitigate this, the moisture in CNCs can be expelled by sublimation *via* the freeze-drying process. However, free-drying results in the aggregation and agglomeration of CNC fibres, making them difficult to disperse in the polymer matrix.

Bagheriasl *et al.* (2018)[3] conducted a comparative study between the direct melt-mixing process and the solution-casting method of preparing CNC-reinforced PLA bionanocomposites. The results from this study indicated that the solution casting method achieved better CNC dispersion, whereas there was significant CNC agglomeration in the bionanocomposites prepared *via* the direct melt-mixing method. Oksman *et al.* (2006)[19] prepared PLA/CNC bionanocomposites by direct liquid-feeding of CNC dispersed in a solution of *N*,*N*-dimethylacetamide (DMAc) containing lithium chloride (LiCl) into PLA melt. Similarly, Herrera *et al.* (2015)[5] dispersed nano cellulose using a mixture of water, acetone, and glycerol triacetate. Afterwards, they prepared well-dispersed PLA bionanocomposites using melt-extrusion and liquid feeding of nano cellulose suspension.[5] However, these methods' drawbacks include toxicity concerns, high cost, limited scalability, and increased hydrolytic degradation of PLA.

This work explores an environmentally friendly and scalable method of producing FDM 3D printable PLA bionanocomposite filaments containing different CNCs loading. Freeze-dried CNCs obtained from forestry waste residues were re-dispersed using a minimal volume of green solvents and without performing any additional chemical modifications. Afterwards, the redispersed CNCs were directly incorporated into PLA during melt-mixing to obtain masterbatches. The melt-mixing was done at a low temperature to minimize the thermal degradation of CNCs and PLA. Optimised amounts of bio-based additives (triacetin and glycerol triacetate) and a food-grade multifunctional chain extender were used as a processing aid, compatibilizer, and plasticizer. Afterwards, a single-screw extruder was used to draw the PLA/CNC bionanocomposites into filaments suitable for 3D printing. The chemical, thermal, rheological, and mechanical properties of the bionanocomposite filaments were investigated. Finally, the 3D printability of the PLA/CNC bionanocomposite filaments was elucidated on a fused deposition modelling (FDM) printer.

2. Materials and methods

2.1. Materials

Polylactic acid (PLA), Ingeo™ PLA6202D, (Mw = 140 kDa, ≤2% D-lactide, fibre grade) was procured from NatureWorks USA. Polyethene glycol, triacetin and a food-safe styrene–acrylic multifunctional chain extender (Joncryl ADR-4368-C) were added to improve flexibility, processability and melt strength. Other solvent-grade chemicals used include ethanol, acetone and ethyl acetate which were procured from Sigma Aldrich.

The freeze-dried cellulose nanocrystals (CNCs) used in this current study were extracted on a pilot scale from sawdust of Eucalyptus grandis, using a propriety technology developed by the Biorefinery Industry Development Facility (BIDF), Natural Resources and the Environment Research Area, Council for Scientific and Industrial Research (CSIR), Durban, South Africa. The freeze-dried CNC were oven dried at 50 °C overnight in an air-circulation oven before use. The transmission electron microscopy (TEM) image of the CNCs has been provided by the supplier and is presented in the ESI.†

2.2. Re-dispersion of cellulose nanocrystals (CNC)

The sublimation of water during the freeze-drying process of CNCs leads to the aggregation and agglomeration of individual fibres due to the high amount of hydrogen bonding.[20] A combination of solvents and mechanical agitation was used to partly destabilize the strong interactions between individual CNC fibres. The fluffy CNCs fibres were carefully transferred into a beaker with the protic and aprotic polar solvents and the mixture was stirred on a magnetic stirrer for 48 hours. The protic and aprotic polar solvent mixture contains acetone, ethanol, and ethyl acetate in the following ratios 3 : 3 : 1. This was followed by sonication for another 24 hours to achieve a fine dispersion. Before use, the re-dispersed CNC was constantly stirred using an overhead stirrer to avoid sedimentation.

2.3. Composition and sample description

The sample containing 100% PLA6202D is denoted as PLA_{100}. Whereas the sample labelled as PLASCE contains PLA6202D with bio-based additives and a food-grade chain extender (CE). Furthermore, the sample description $PLACNC_{0.1\%}$, $PLACNC_{0.5\%}$, and $PLACNC_{1\%}$ represents the bionanocomposite samples containing 0.1%, 0.5% and 1% cellulose nanocrystals (CNCs). Each bionanocomposite contains equal amounts of additives and chain extender. Table 1 shows the final composition of each sample per mixing cycle.

2.4. Preparation of PLA/CNC bionanocomposites

The melt-mixing of bionanocomposites was conducted using a Haake™ Rheomix QC internal mixer (Thermo Fisher Scientific, Waltham, MA USA) set at 165 °C at 75% fill factor. The PLA was

Table 1 Formulation for PLA and bionanocomposites

	Composition (%)			
Sample description	PLA	Biobased additives	CNCs	Mixing time (minutes)
PLA_{100}[a]	100	0	0	6
PLASCE[b]	89	11	0	6
$PLACNC_{0.1\%}$[c]	88.9	11	0.1	8
$PLACNC_{0.5\%}$[c]	88.5	11	0.5	10
$PLACNC_{1\%}$[c]	88	11	1.0	14

[a] Virgin PLA. [b] PLA containing plasticizer, chain extender. [c] PLA containing plasticizer, chain extender and cellulose nanocrystals.

divided into two parts and mixed in 2-steps: firstly, PLA alone was fed into the mixing chamber and mixed for 2 min at 30 rpm. Afterwards, the remaining PLA and additives (TA/PEG/CE) were carefully added into the mixing chamber and mixed for additional 3 min at 60 rpm to complete the 2nd mixing step. The evolution of torque on the mixer's rotors and mixing temperature as a function of time was plotted by Rheomix software as seen in Fig. 1(a and b). The additives improved processibility hence the significant reduction in torque [Nm] as seen in Fig. 1. To make the PLA/CNC bionanocomposites, the re-dispersed nano cellulose was introduced after the first mixing step. A pneumatically controlled laboratory hot press set at 165 °C was used to compress each specimen into approximately 0.3 mm sheets. The melt-mixed specimen was placed between Teflon sheets and compressed for 1 minute. Afterwards, the compressed sheets were air-cooled and shredded into extrudable pellets. The shredded samples were then dried at 50 °C for 24 h and vacuumed and sealed in zip-lock bags for further processing.

2.5. Preparation of 3D printable filaments

The monofilaments of the various samples were drawn using a compact 3D filament extruder system (Felfil evo, Felfil, Torino). The extruder features a 2 mm nozzle and a K100 steel extrusion screw with a conic profile for an improved compression rate (12.7 L/D ratio). The extrusion temperature was set at 175 °C, and the extrusion speed was varied between 5–7 rpm depending on the sample. The filaments were extruded and spooled using a Felfil spooler system (Felfil, Torino). The spooler system also features a 4 radial high-speed fan array, that cools down the filaments before winding. Fig. 2 below shows the filament extrusion setup. Finally, the filaments were air dried in a convection oven set at 50 °C for 24 h and stored in vacuumed sealed bags for further processing.

2.6. 3D printing application

3D printing was performed using a desktop Fused Deposition Modelling (FDM) 3D printer (Wanhao Duplicator i3 plus) fitted with a 0.4 mm nozzle. Printing conditions were as follows, bed temperature of 50 °C, print speed of 60 mm s^{-1}, 2 perimeter walls, 0 top and bottom layers, and a primary layer height of 0.26 mm. The printing temperature was optimized using a temperature tower calibration step and would be discussed later. A circular disk of 25 mm diameter and 1.5 mm thickness was 3D printed and used for melt-rheological analysis. All

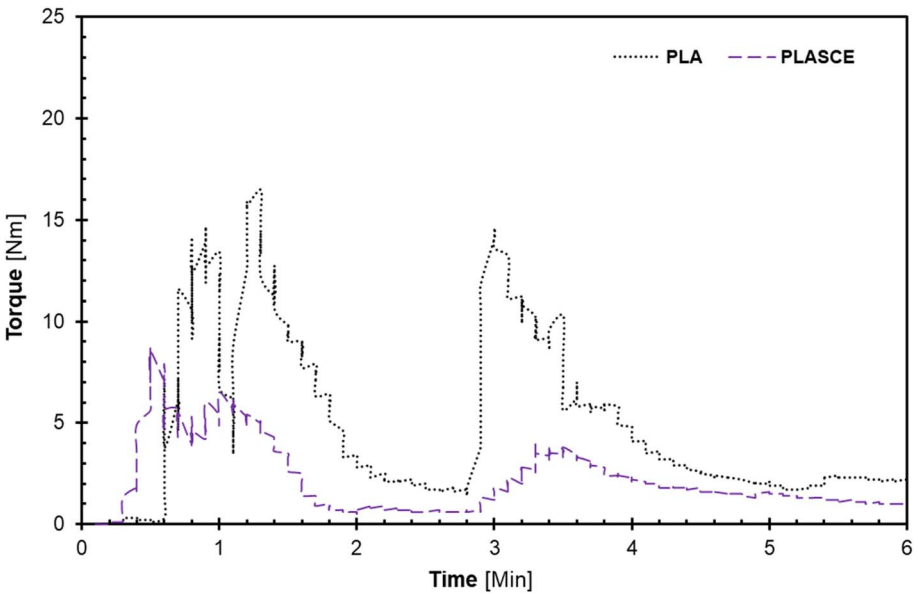

Fig. 1 A plot of torque *vs.* time plots during melt-mixing of PLA and plasticized PLA; (a) first, and (b) second mixing regimen.

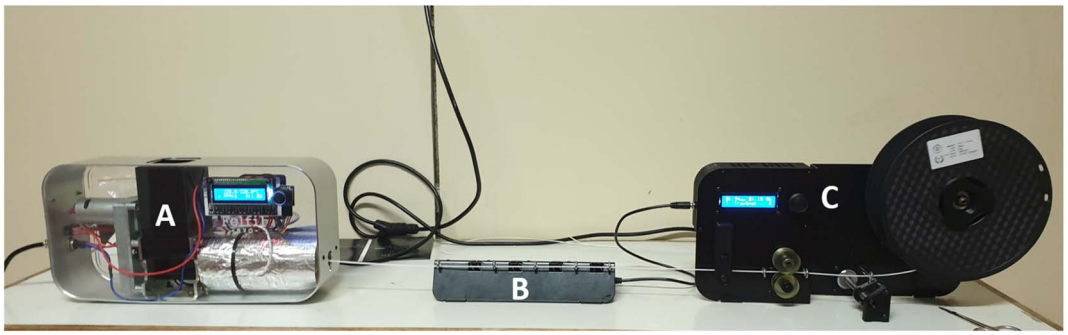

Fig. 2 Filament extrusion set-up, (A) single screw extruder, (B) spooling fan, (C) filament spooler.

specimens were 3D printed lying flat with 90° raster angles, infill directions running parallel to the length in the XY direction. Simply3D® slicing software was used to slice the various STL files and program the 3D printing parameters.

3. Characterization techniques

3.1. Fourier Transform Infrared Spectroscopy (FTIR)

The cellulose nanocrystals (CNCss) were analysed using a TENSOR II FTIR spectrophotometer (BRUKER, Billerica, MA, USA) fitted with a pure diamond crystal and Platinum Attenuated Total Reflectance (ATR) accessory. The FTIR spectrum was recorded by scanning the sample 30 times at 1 cm^{-1} resolution between 4000 and 400 cm^{-1}. CNCs were collected from the top, middle and bottom areas and tested to check for reproducibility. FTIR spectroscopy was also used to analyse the chemical structure of all the PLA and PLA/CNC bionanocomposite filaments.

3.2. Crystallinity analysis using X-ray powder diffraction (XRD)

A D2 PHASER benchtop powder X-ray diffractometer (BRUKER Billerica, MA, USA) was used to elucidate the crystallinity of the freeze-dried CNC. The samples were dried at 50 °C for 12 hours, afterwards the X-ray diffraction (XRD) pattern was measured over the angular $2\theta = 5$–40° range with a scanning step of 0.02°/step and 4 s per step with sample rotations using a Cu k-α1 radiation source (λ = 0.15406 nm). A silicon (Si) zero background sample holder was used, and the sample rotated in the horizontal plane at 10 rpm. In addition, a 3 mm air scatter slit was in place to reduce the low-angle erroneous air scattering that could be misinterpreted. After subtracting the air scattering, the diffraction patterns acquired were resolved into crystalline reflections and non-crystalline scattering using DIFFRAC.EVA software. The crystallinity index (I_c) was estimated using the semi-empirical method proposed by Segal *et al.*[29] eqn (1);

$$I_c = \frac{I_{200} - I_{AM}}{I_{200}} \times 100 \quad (1)$$

The I_{200} represents the height maximum diffraction peak of the (200) lattice (at $2\theta = 21°$) and the I_{AM} was deduced from the minimum between the 200 and 110 lattice peaks (I_{AM}, $2\theta = 18°$). The I_{200} represents both the crystalline and amorphous cellulose components, while I_{AM} represents only the amorphous component. The crystallite size was calculated using the Scherrer equation as represented in eqn (2):[30]

$$D_{hkl} = \frac{0.9\lambda}{\beta \cos \theta} \quad (2)$$

where D_{hkl} = crystallite size in the direction normal to the *hkl* lattice planes, λ = X-ray radiation wavelength (1.542 Å), β = full width at half-maximum (FWHM) of the diffraction peak in radians, and θ = corresponding Bragg angle.

3.3. Polarised optical microscopy (POM)

Samples of the re-dispersed CNCs were examined under a Leica S6D light microscope (Leica Microsystems, Germany). A few drops of the CNCs sample were placed on a glass slide and allowed to dry in a desiccator. Afterwards, the glass slide containing the CNCs specimen was viewed under polarised and unpolarised light. Subsequently, images were captured using a 3.1-megapixel Leica EC3 colour camera (Leica Microsystems, Germany) at 64× magnification.

3.4. Scanning electron microscopy

High-resolution images of filament cross-sections were acquired using a JSM-IT100 InTouchScope™ scanning electron microscope (SEM) (JEOL Ltd. Japan). Filaments were cryo-fractured in liquid nitrogen and then attached to a metal substrate using double-sided carbon tape. Gold coating of the filament specimen was performed using a DESK V sputter coater (DENTONVACUUM, NJ, USA).

3.5. Thermal analysis

3.5.1. Thermal degradation of cellulose nanocrystals (CNCs). Thermal degradation analysis of the cellulose nanocrystal (CNCs) specimen was conducted on a thermogravimetric analyser (Discovery Series TG 5500, TA Instrument). Platinum samples and reference pans were used for this experiment. About ~4 mg of CNCs sample was heated at a rate of 10 °C min^{-1} from ambient

temperature (~20 °C) to 600 °C. This experiment was conducted under a nitrogen atmosphere at a gas flow rate of 100 mL min^{-1}.

3.5.2. Melt crystallization analysis of bionanocomposites. The melt-crystallization behaviour of the bionanocomposites was studied using a differential scanning calorimeter (Discovery series, TA Instruments). About ~1.5 mg sample was weighed and sealed in an aluminium pan whereas an empty aluminium pan was used as reference. The sample was heated from 30 °C to 200 °C at a rate of 20 °C min^{-1} to erase the previous heat history. Afterwards, the melt crystallization behaviour was measured by cooling the samples at 5 °C min^{-1} from 200 °C to 0 °C. This was followed by a heating scan from 0 °C to 200 °C at a heating rate of 20 °C min^{-1}. The heating and cooling cycles were conducted under nitrogen as the purge gas, with a flow rate of 25 mL min^{-1} for all samples. The first heating cycle was performed on all the samples to erase the previous heat history.

3.5.3. Thermal stability analysis of bionanocomposite filaments. The thermal behaviour of all filament samples was studied on a simultaneous differential scanning calorimeter and thermogravimetric analyser (DSC-TGA) (SDT Q600, TA instrument, New Castle, USA). Samples weighing about ~6.5 mg were carefully placed in ceramic pans and heated from ambient temperature (~25 °C) until 600 °C at a 10 °C min^{-1} heating rate under a nitrogen purge atmosphere at a flow rate of 100 mL min^{-1}.

3.6. Rheological analysis of bionanocomposites

The melt rheological analysis was conducted using an Anton-Paar modular compact rheometer (MCR-502) fitted with a 25 mm (diameter) parallel plate measuring system and a Peltier temperature control system. Circular-shaped (25 mm diameter and 1.5 mm thickness) test specimens were 3D printed for this experiment. Strain sweep measurements were conducted in the 0.1–100% deformation range at 10 rad s^{-1} to determine the linear viscoelastic region (LVR). Based on the LVR, dynamic frequency sweep measurements (0.1–100 rad s^{-1}) were performed on all the samples at a constant temperature (190 °C) fixed strain (1%) and 1 mm gap size. Low-temperature drying and conditioning of the test specimen were performed at 45 °C for 5 hours before rheological analysis to avoid moisture absorption and thermal ageing. Each sample was analysed in triplicates and the data presented is the averaged result obtained from each sample.

3.7. Tensile analysis of filaments

Tensile analysis was performed using a Tinius Olsen tensile tester fitted with a loadcell of 10 kN loadcell. A gauge length of 25 mm was set throughout the analysis. Filaments were tested at a 50 mm min^{-1} speed according to ASTM D638 standard.

4. Results and discussion

4.1. Morphological analysis of re-dispersed cellulose nanocrystals

Fig. 3 shows the pictures of freeze-dried cellulose nanocrystals (CNCs) before and after re-dispersion in a mixture of polar protic (ethanol) and aprotic (acetone and ethyl acetate) solvents. The re-dispersion was achieved using a mixture of protic (ethanol) and aprotic (acetone and ethyl acetate) polar solvents. The mechanical stirring and ultra-sonication performed during this step aided the diffusion of solvents onto the surfaces of the CNCs bundles. Furthermore, the strong hydrogen bonding between the cellulose fibres became weakened because of the interactions with the polar solvents. The dissolution of cellulose in a mixture of aprotic and protic solvents involves solvent diffusion and chain disentanglement processes, made possible because of the weakening of the strong hydrogen bonds between agglomerated CNCs.[31] Fortunati *et al.* (2012)[20] employed the use of a surfactant to mitigate the agglomeration of CNC during the freeze-drying process, however, the process required additional use of chemicals.

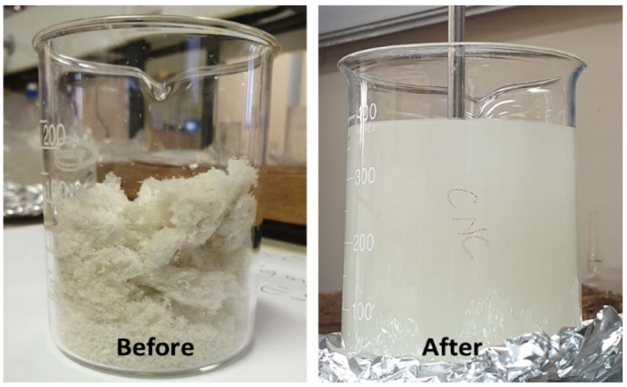

Fig. 3 Freeze-dried cellulose nanocrystals (CNCs) before and after re-dispersion in a mixture of polar protic and aprotic solvents.

The optical microscopy image presented in Fig. 4A revealed the size anisotropy of CNCs fibres after redispersion, whereas the image captured under polarised light in Fig. 4B reveals the birefringence of aggregated cellulose nanocrystals. The observed birefringence is characteristic of CNCs; this behaviour emanates from the refraction of polarised light passing through highly ordered cellulose crystals.[32]

4.2. Chemical composition analysis of cellulose nanocrystals

The FTIR spectrum of the freeze-dried cellulose nanocrystals (CNCs) and Eucalyptus saw-dust (ESD) are represented in Fig. 5. The CNCs show characteristic adsorption of chemical functional groups present in cellulosic materials. The prominent peaks include –O–H stretching vibrations responsible for the broad bands ranging from 3000–3600 cm^{-1}. C–H stretching of methylene groups in cellulose around 2898.66 cm^{-1}. Also, the peak around 1620 cm^{-1} is consistent with the –O–H bending vibrations of absorbed water and hydrogen-bonded hydroxyl groups of cellulose.[33] The peak around 1450 cm^{-1} is assigned to $-CH_2$ bending vibrations and the peak at 1339 cm^{-1} is assigned to –C–H asymmetric deformation of the crystalline domains.[34] In the fingerprint region, the stretching vibrations from the –C–O–C– glucose and pyranose ring skeleton of cellulose are assigned to the 1160 and 1047 cm^{-1} peaks.[35] Elanthikkal *et al.*[36] suggested that the increase in the vibration observed at these peaks corresponds with

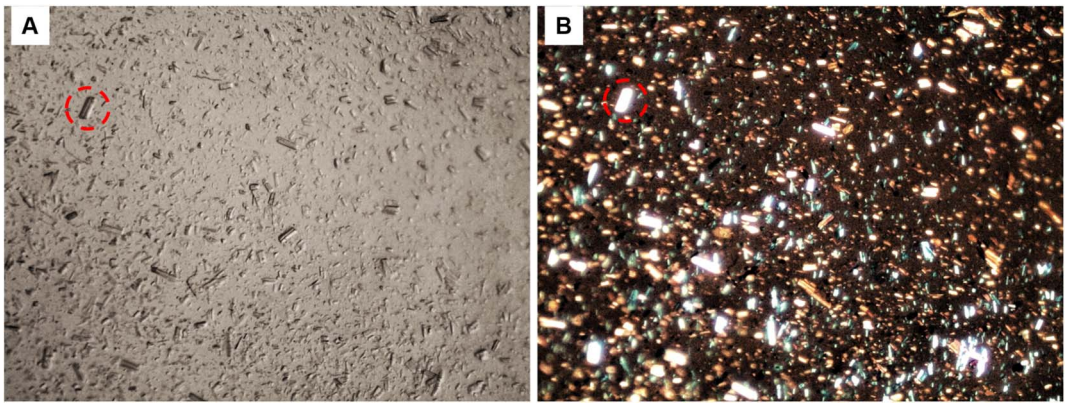

Fig. 4 Optical microscopy image of re-dispersed cellulose nanocrystals (CNCs); (A), high contrast image under normal light, (B) CNCs showing birefringence under polarised light (64× magnification).

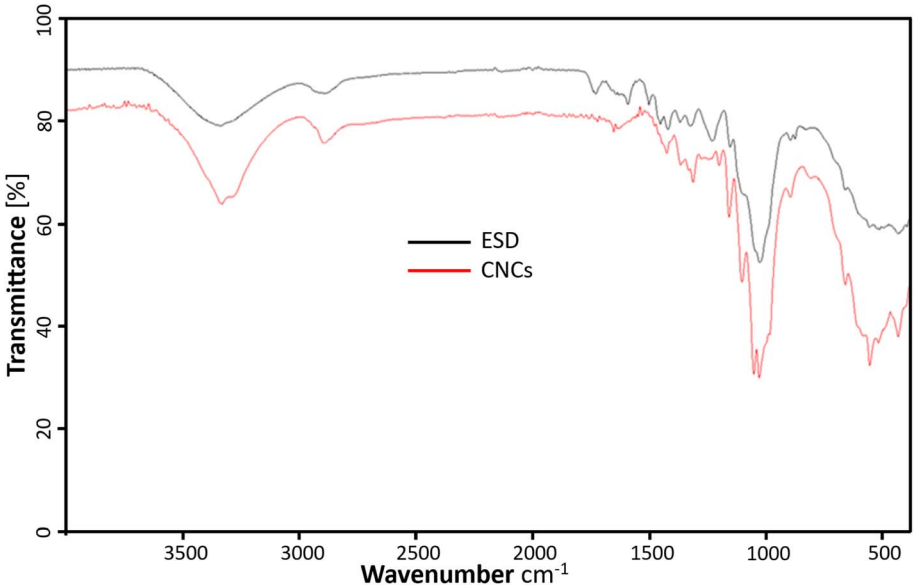

Fig. 5 ATR-FTIR profiles showing the chemical composition of cellulose nanocrystals (red), and Eucalyptus grandis saw dust (black).

increasing cellulose content. Furthermore, the C–O stretching of the β-glycosidic linkages between glucose rings in cellulose is attributed to the small peak at 897 cm^{-1}.[37] The characteristic aromatic ring vibration of lignin usually seen around 1230.54 cm^{-1} and 1503.84 cm^{-1} are absent in CNCs but present in ESD.[16] Also, the C=O stretching of hemicellulose and lignin (1600–1750 cm^{-1}) present in ESD is almost negligible in the spectrum of CNCs. This indicates the lignin and hemicellulose components were removed during the extraction of CNCs.[16,38] There is no evidence of surface-absorbed sulfate groups[39] as the characteristic 800 cm^{-1} peak from S–O bond stretching vibrations is not noticeable.

4.3. XRD crystallinity analysis of cellulose nanocrystals (CNCs)

The XRD diffractograms of the freeze-dried CNCs and eucalyptus saw dust (ESD) exhibited patterns consistent with the crystalline structure of cellulose type I_β (ref. 39) (Fig. 6). The peaks observed at 2θ = 14–17°, 23° and 35° are assigned to the (1−10) and (110), (200) and (004) lattice planes of monoclinic cellulose type I_β lattice.[40,41] The empirically determined crystallinity index (I_c%) was calculated to be 70% for CNCs, and 71.92% for ESD. The slight reduction in I_c% indicates minimal loss of crystalline domains during the extraction of cellulose nanocrystals. Noteworthily, I_c% only describes the relative among of crystalline and amorphous domains present, so it can only be used as a basis of comparison as it provides no information about the crystallinity of the crystalline region or the size of crystallites.[29,39] The crystallite size (D_{hkl}) was deduced using the Scherrer equation and was found to be 36.6 Å for CNCs compared to 29.55 Å for ESD. The larger crystallite size indicates the successful removal of amorphous cellulose.

4.4. Thermal stability analysis of cellulose nanocrystals (CNCs)

The thermal degradation profile of the freeze-dried cellulose nanocrystal (CNCs) is represented in Fig. 7. The

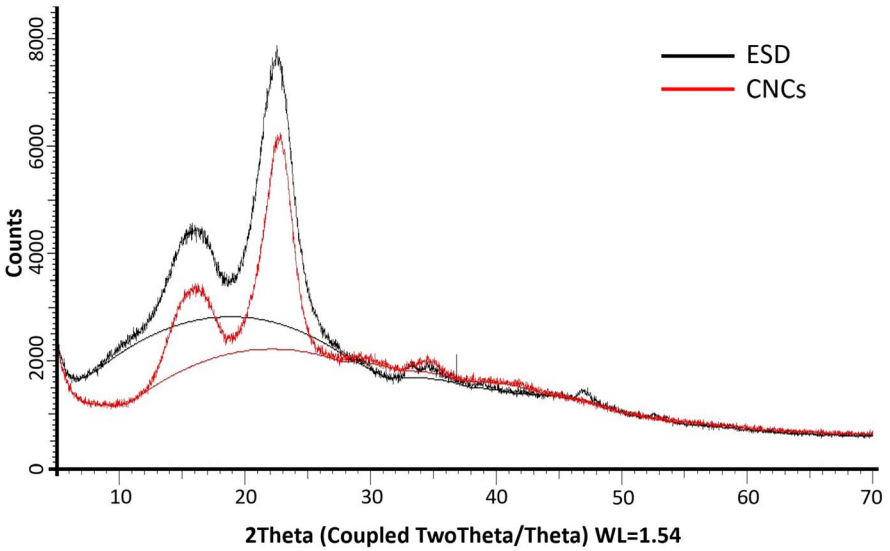

Fig. 6 PXRD patterns of Eucalyptus grandis saw dust (black) and extracted cellulose nanocrystals (red); (solid lines between $2\theta = 10°$ and 30° show amorphous hump).

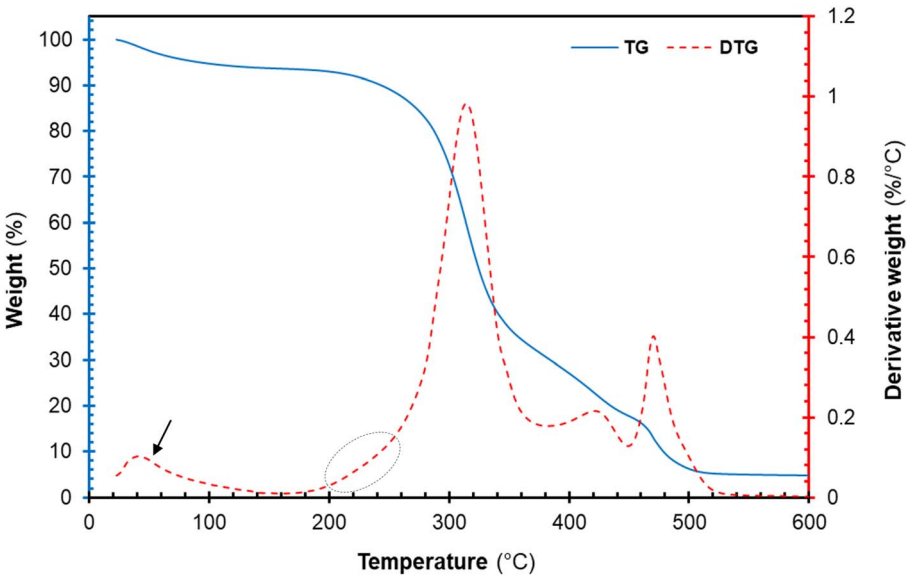

Fig. 7 Thermal decomposition profile of cellulose nanocrystals (CNCs): thermogravimetric curves (solid blue line), derivative TG curve (red broken lines).

thermogravimetric (TG) and derivative thermogravimetric (DTG) plots of CNCs displayed an early weight loss around 40–100 °C. This early weight loss is attributed to the evaporation of volatiles and moistures present in each sample.[16,42] Furthermore, the TG and DTG plots of the cellulose component displayed multi-step degradation as seen in Fig. 7. The early decomposition (circled in Fig. 7) is attributed to the thermal degradation of highly accessible sulphated cellulose regions resulting from excessive acid hydrolysis.[16,43] The sulphate groups present on the surfaces of CNCs are known to catalyse the thermal degradation process.[20] Roman and Winter (2004)[44] reported that the introduction of sulphate groups on the surface of CNCs during sulphuric acid hydrolysis significantly lowers the activation energies of thermal degradation. Nonetheless, the thermal degradation of cellulose glycosyl regions was not affected by sulphuric acid occurring at 315.54 °C. Furthermore, the peaks around 400–480 °C are attributed to the decomposition of thermal stable pyrolysis products formed during the degradation of the cellulose region charred residues occurring around. Overall, the degradation of the CNCs proceeded *via* dehydration, depolymerization and decomposition of glycosyl regions, similar to observations reported in the literature.[16,42]

4.5. Analysis of the chemical structure of bionanocomposite filaments

Fig. 8 shows the FTIR spectra of the neat PLA, plasticized PLA (PLASCE) and the PLA/CNCs bionanocomposite filaments. All the specimens exhibited transmittance peaks consistent with the chemical functional groups present in PLA. The peaks in the 3050–2900 cm^{-1} range are assigned to the C–H stretching. The C═O stretching and $-CH_3$ asymmetric bending vibrations are assigned to the peaks at 1750 cm^{-1} and 1450 cm^{-1} respectively. The 1260 cm^{-1} peak is assigned to carbonyl (C═O) bending vibrations, whilst the skeletal stretching vibrations of the PLA-ester groups (C–O–C) are assigned to 1200–700 cm^{-1} peaks. Additionally, the peaks at 960 cm^{-1} and 925 cm^{-1} seen in the FTIR spectra of bionanocomposite filaments are assigned to amorphous and crystalline vibrations of PLA.[45] The filaments containing CNCs, and additives all exhibited higher carbonyl signals around 1750 cm^{-1}, whilst their methyl group signals (3050–2900 cm^{-1}) were reduced. This observation is attributed to the reaction between PLA and the multifunctional chain extender, which formed new carbonyl bonds. Grigora *et al.*

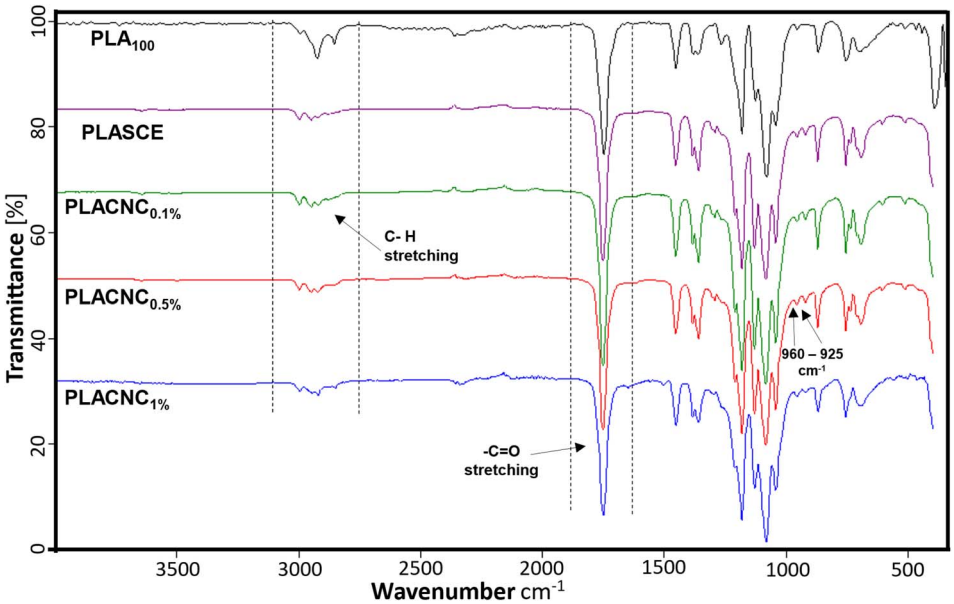

Fig. 8 Chemical composition of PLA and PLA/CNC bionanocomposites filaments.

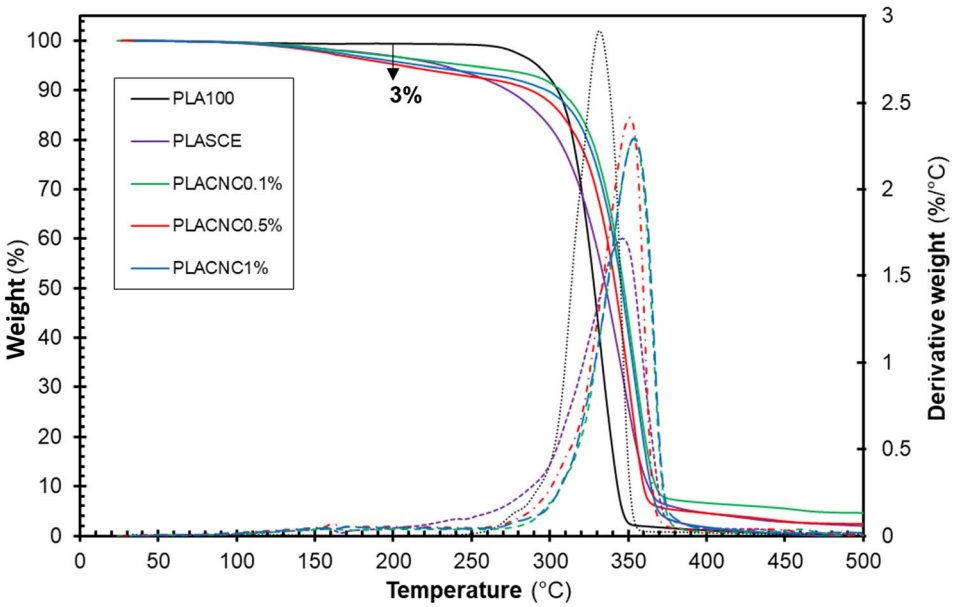

Fig. 9 Thermal decomposition profiles showing thermogravimetric (TG) and derivative (DTG) curves of the PLA and bionanocomposites filaments.

(2021)[46] also reported a similar observation after studying the influence of multifunctional chain extenders on the chemical structure of PLA using FTIR spectroscopy.

4.6. Thermal analysis of PLA/CNC bionanocomposite filaments

Fig. 9 shows the thermogravimetric weight loss (TG) and derivative (DTG) curves of the filaments of each specimen. The plasticized PLA (PLASCE) and the bionanocomposite filaments all exhibited a weight loss event around 150 °C. This weight loss is attributed to the evaporation of the plasticizer and is absent in the TG/DTG profile of the neat PLA (PLA_{100}). However, only 3 wt% of the plasticizer was lost at 200 °C, which is above the maximum 3D printing temperature used for bionanocomposite. The main weight loss started around 270 °C and represents the onset of thermal degradation of cellulose nanocrystals and PLA matrix. The main degradation peak occurred at 331.8 °C for neat PLA (PLA_{100}), 346.79 °C for the plasticized sample (PLASCE) and around 350 °C for the samples containing CNCs. A comparison of the peak degradation temperature reveals a ~20 °C improvement upon the addition of CNCs. The increase in thermal stability of PLA upon incorporating CNCs has been reported elsewhere.[23,47] Furthermore, the diminished height of the DTG curve for the bio-based plasticized sample (PLASCE) is attributed to decreased rate of thermal decomposition. However, the height of the DTG curves of the bionanocomposite specimens infers that the addition of CNCs improved the rate of thermal degradation.

4.7. Melt-crystallization analysis of PLA/CNC biocomposites

The differential calorimetric profile in Fig. 10 shows the first heating run, cooling and the 2nd heating run of PLA_{100}. Thermal events consistent with PLA such as glass transition (T_g ~ 62.72 °C), cold crystallization (T_{cc} ~ 100.19 °C), crystalline melt temperature (T_m ~ 167.47 °C) and cooling crystallization (T_c ~ 94.18 °C) were recorded. The endotherm is visible just after T_g has been linked with a complex thermal ageing phenomenon.[27] However, this endotherm is largely invisible in the second heating run as the previous history was erased. The additional exothermic peak which occurred just before the main melting point, is attributed to the additional melting/recrystallization mechanism. The percentage degree of crystallinity from the cooling and second heating run was mathematically deduced using the equations below.

$$\chi = \frac{(\Delta H_m - \Delta H_{cc})}{\Delta H_m^{\circ}(1 - \varnothing)} \times 100 \quad (3)$$

$$\chi_c = \frac{(\Delta H_c)}{\Delta H_m^{\circ}(1 - \varnothing)} \times 100 \quad (4)$$

where χ_c is the crystallinity of the cooling cycle (eqn (3)) and χ refers to the overall degree of crystallinity after the 2nd heating cycle (eqn (4)), ΔH_m is the enthalpy of melting for the 2nd heating run, ΔH_c is the enthalpy of crystallization for the cooling run and ΔH_{cc} is the enthalpy of cold crystallization. The values of ΔH_m, ΔH_c and ΔH_{cc} were deduced by integrating the area of the thermal transition. ΔH_m° is the melting enthalpy of a 100% crystalline PLA reported as 93 J g^{-1} in literature,[4] whereas $(1 - \varnothing)$ represents the mass fraction of PLA. Table 2 shows all the melt-crystallization information obtained from the DSC analysis.

The results in Table 2 reveal a slight delay in the onset of melt crystallization temperature (T_c) after the addition of CNCs. The delay in T_c is more prominent in the specimen containing 1% CNCs (T_c ~ 89.15 °C). The crystallization behaviour of polymers in the presence of nanoparticles is controlled by two competing phenomena. The first phenomenon occurs when the nanoparticles act as nucleation sites for crystal growth, thus resulting in increased crystallinity.[27] The second phenomenon

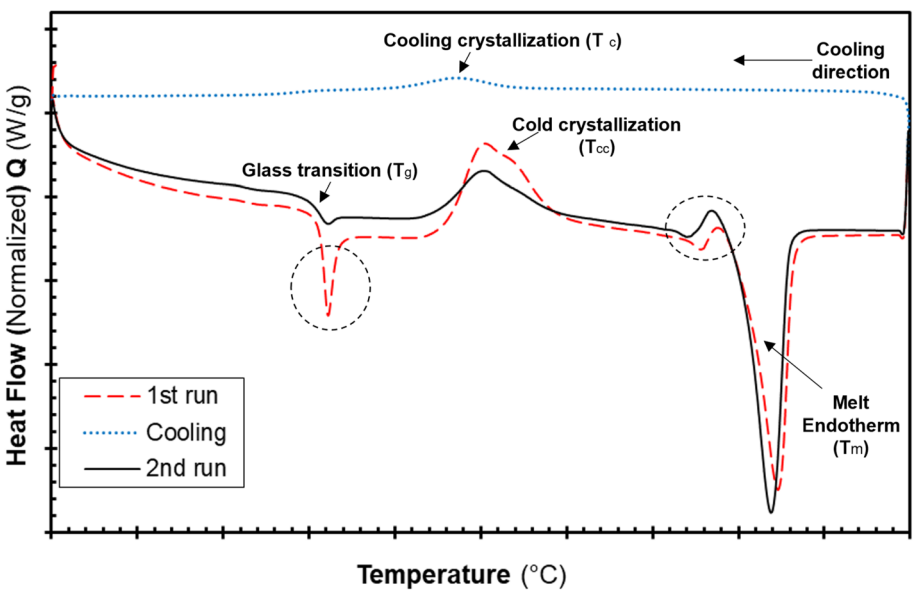

Fig. 10 DSC thermograms of the neat PLA filaments showing the first, cooling and second heating runs.

Table 2 DSC data for the cooling and second heating run PLA and PLA/CNC bionanocomposites

	Cooling run			2nd heating run				Crystallinity	Glass transition
Sample description	T_c (°C)	ΔH_c (J g^{-1})	χ_c (%)	T_{cc} (°C)	ΔH_{cc} (J g^{-1})	T_m (°C)	ΔH_m (J g^{-1})	X (%)	T_g (°C)
PLA_{100}	94.18	11.40	12.26	100.19	12.09	167.47	40.34	30.38	62.72
PLASCE	97.11	18.62	20.02	102.41	4.27	166.89	27.96	22.67	56.72
$PLACNC_{0.1\%}$	90.62	16.28	17.51	103.53	12.88	167	29.79	16.17	56.29
$PLACNC_{0.5\%}$	93.33	25.89	27.84	97.05	6.068	165.88	31.17	23.89	54.48
$PLACNC_{1\%}$	89.15	21.7	23.33	95.47	7.457	166.63	35.3	26.35	49.22

leads to lower crystallinity as the nanoparticles physically hinder crystal growth.[48] Although the CNCs present in the bionanocomposites hindered the migration and diffusion of polymer chains to the surface of the growing crystal. The slight decrease in crystallization temperature and the broad T_c exotherms in Fig. 11 is attributed to the second phenomenon. The χ_c of the neat PLA was determined to be 12.26%; however, the specimens containing CNCs exhibited higher crystallization during the cooling run. Compared to PLA_{100}, their χ_c increased by 5%, 15% and 11% for $PLACNC_{0.1\%}$, $PLACNC_{0.5\%}$, $PLACNC_{1\%}$ respectively. This observation agrees with the results presented by Bagheriasl *et al.* (2018).[49]

Fig. 12 shows the evolution of thermal events during the second heating run for all the specimens. The glass transition temperature (T_g) of the plasticized specimen (PLASCE) and the bionanocomposites were barely noticeable. This is attributed to the increased mobility of the PLA chains due to the lubricating effect of the plasticizer. The lubricating effect also resulted in the lowering of the T_g temperatures in all the samples containing plasticizer as shown in Table 2. Also, Fig. 12 shows that the PLA crystallites' melting endotherms (T_m) occurred at around 166 °C in all the samples. However, PLA_{100} exhibited the highest melting enthalpy ($\Delta H_m \sim 40.34$ J g^{-1}) due to the higher cold crystallization (T_{cc}) behaviour and the residual crystallization that occurred just before the onset of melting. The high ΔH_m corresponded with the increased crystallinity of the PLA100 specimen ($\chi \sim 30.38\%$). Meanwhile, the plasticized specimen (PLASCE) exhibited the lowest melting enthalpy ($\Delta H_m \sim 27.96$ J g^{-1}). The incorporation of CNCs into plasticized PLA resulted in slightly higher melting enthalpy compared to plasticized PLA where ΔH_m was calculated as ~29.79, 31.17 and 35.30 J g^{-1} for samples containing 0.1, 0.5 and 1% CNC respectively. Furthermore, the plasticized PLASCE and bionanocomposites exhibited lower overall percentage crystallinity (χ) which was calculated from the second melting endotherm. The low overall crystallinity (χ) is attributed to the slow cold crystallization (T_{cc}) process caused by the lubricating effect of the plasticizer.

4.8. Tensile analysis of PLA/CNC biocomposite filaments

The tensile properties of the bionanocomposite filaments were compared to the neat (PLA_{100}) and plasticized (PLASCE) filaments. Table 3 lists the tensile strength, elongation at the break and maximum breaking force of the analysed filament materials. The neat PLA filament (PLA_{100}) was very brittle and repeatedly broke

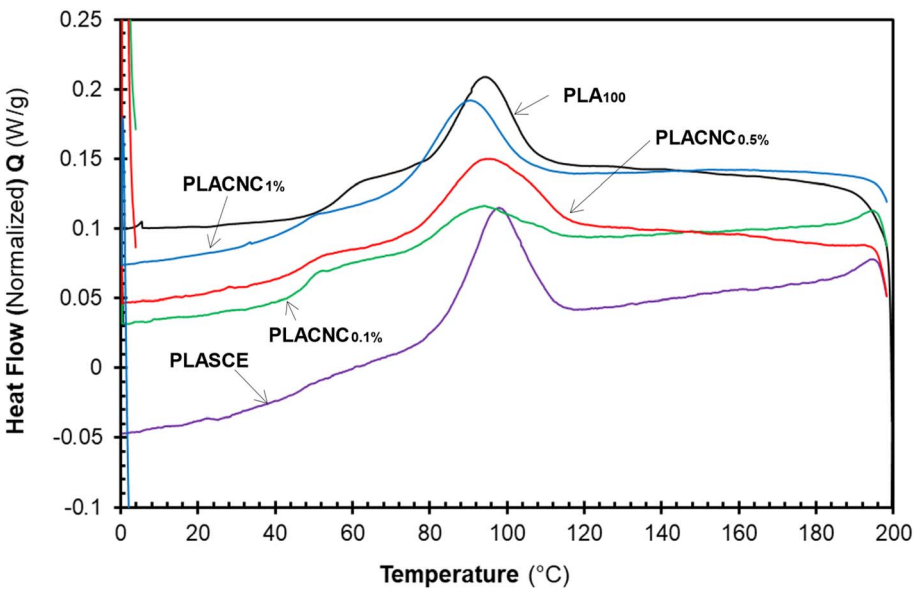

Fig. 11 DSC cooling curves showing the melt crystallization behaviour of the PLA and bionanocomposites filaments.

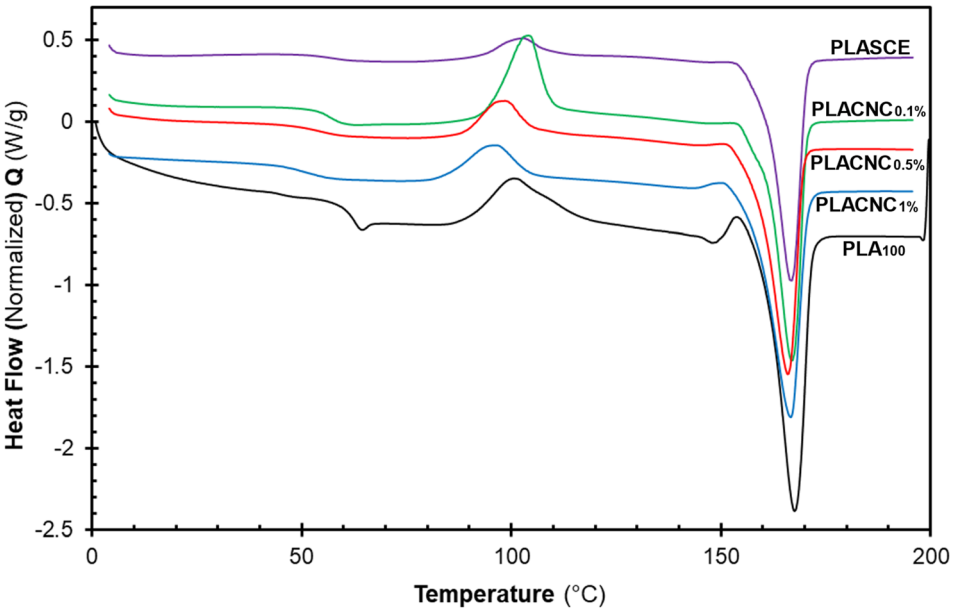

Fig. 12 The evolution of thermal events in the second heating cycle of the PLA and bionanocomposites filaments.

Table 3 Summary of the tensile results of the PLA and bionanocomposites filaments

Sample description	CNCs[a] content (wt%)	Tensile strength (MPa)	Maximum force (*N*)	Elongation at break (%)
PLA_{100}	0	22.5 (±3.80)	53.5 (±9.00)	0.3 (±0.05)
PLASCE	0	28.9 (±1.52)	62.7 (±6.03)	15.8 (±4.34)
$PLACNC_{0.1\%}$	0.1	35.3 (±1.79)	78.4 (±18.3)	15.4 (±4.31)
$PLACNC_{0.5\%}$	0.5	33.4 (±2.07)	71.3 (±2.38)	13.1 (±4.61)
$PLACNC_{1\%}$	1	35.1 (±4.07)	86.9 (±8.42)	25.5 (±5.38)

[a] Cellulose nanocrystal.

during tensile analysis. However, the CNCs-reinforced PLA bionanocomposites filaments exhibited improved flexibility and tensile strength as shown in Table 3. As expected, the maximum force at break (*N*) was higher for samples with improved tensile strength. The improvements in tensile strength and flexibility are attributed to the homogenous dispersion of CNCs, good interfacial interactions and successful plasticization. Additionally, CNCs could have also improved the tensile properties of PLA by influencing the formation of structurally stable crystallites during the cooling process.[50] The neat PLA filament (PLA_{100}) exhibited a tensile strength of 22.5 ± 3.8 MPa and 0.3% elongation at break. Meanwhile, the bionanocomposite filaments exhibited significant improvement in tensile strength of 35.3 ± 1.79 ($PLACNC_{0.1\%}$), 33.4 ± 2.07 ($PLACNC_{0.5\%}$), and 35.1 ± 4.07 ($PLACNC_{1\%}$) MPa respectively. The observed increase in tensile strength is attributed to the effective stress transfer from the PLA matrix to the CNCs, which is in agreement with similar findings reported in the literature.[24,28]

4.9. Analysis of PLA and PLA/CNC bionanocomposite filaments

The poor melt strength of virgin PLA affects its draw ability during filament production. This directly affects the final diameter and ovality (*i.e.*, the deviation from circularity) of PLA filaments. Also, the filaments produced using PLA alone were very brittle and unsuitable for FDM 3D printing. These issues are undesirable as they can lead to inadequate extrusion and cause catastrophic breakage of filaments during FDM 3D printing. The biobased additives (triacetin/polyethylene glycol) and food-safe-multifunctional chain extender (Joncryl CE) were added to mitigate these issues. Fig. 13 shows that the modification resulted in a noticeable improvement in the melt strength of PLA during filament extrusion. The minimal ovality seen in the scanning electron microscopy images presented in Fig. 13 also revealed improved filament roundness for the modified specimen. The biobased additives served as a processing aid, plasticizer and compatibilizer, whereas the multifunctional chain extender (Joncryl CE) improved the melt strength of the PLA during filament production. The improvement in melt strength has been attributed to the formation of a covalent bond between the hydroxyl of PLA and the epoxide group of the Joncryl CE.[46] Also, the addition of Joncryl CE results in increased PLA molecular weight and mitigates the occurrence of thermos-hydrolytic degradation.[46,51,52] Other major contributors to the diameter inconsistencies during filament production include feeding rate, compression, extrusion speed, temperature, rate of cooling, and filament winding speed.

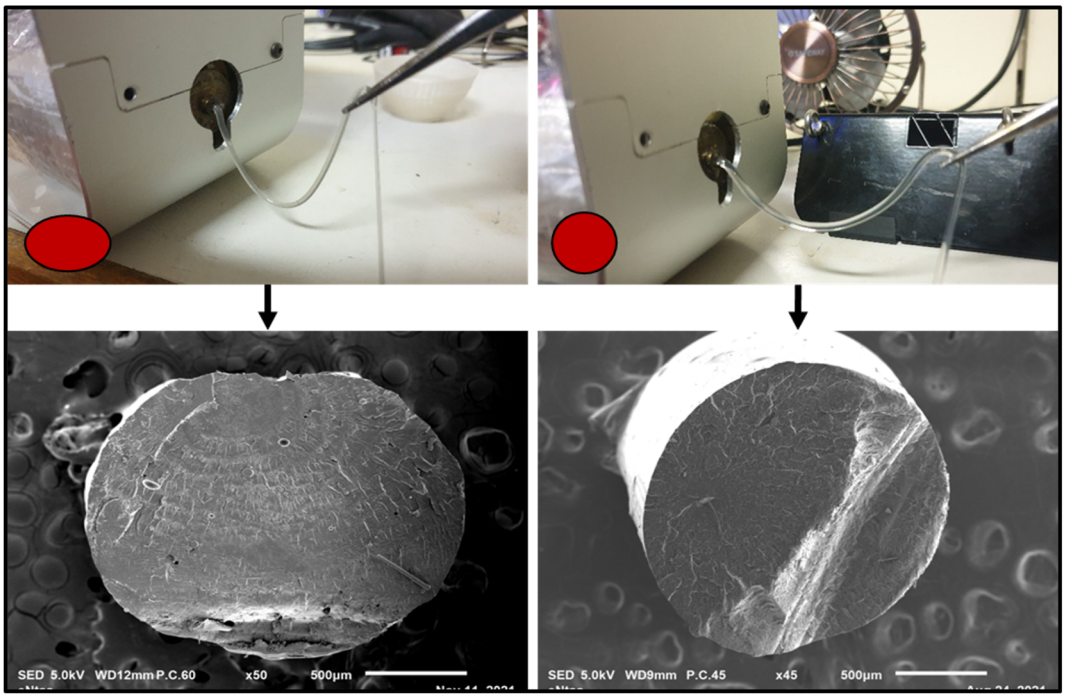

Fig. 13 Enhanced melt strength during filament extrusion: minimal drooping of filament during extrusion.

Fig. 14 shows the higher SEM magnification images of the cryo-fractured bionanocomposite filament. The surface topography shows distinct brittle failure patterns which were expected since the filaments were cryo-fractured. Also, the SEM image reveals bundles of CNCs embedded into the PLA matrix. A few locations where CNCs got pulled out of the PLA matrix are also visible in figure. The average flat width of the CNCs embedded in the PLA matrix was 1.26 micrometres. The small oval-shaped voids indicate the clear boundary between the phased separated plasticizer and PLA matrix. The plasticizer only permeates and interacts with the amorphous domains in PLA; whereas its phase separates from the PLA crystalline domains.[53]

Although the real-time filament diameter was displayed by the Felfil™ filament spooler, the system is not equipped to store

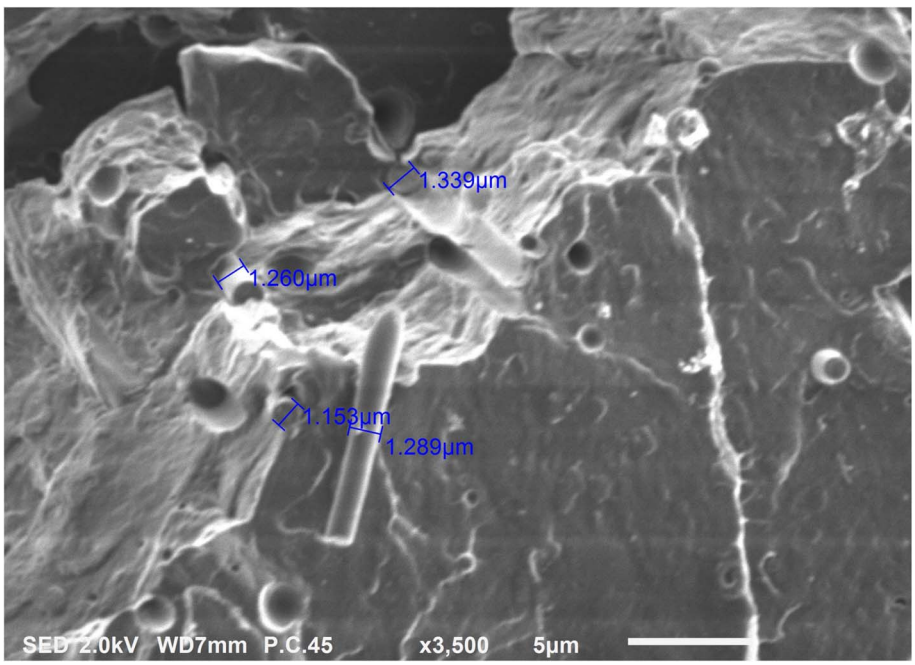

Fig. 14 Higher magnification SEM image of PLA/CNC bionanocomposite filament.

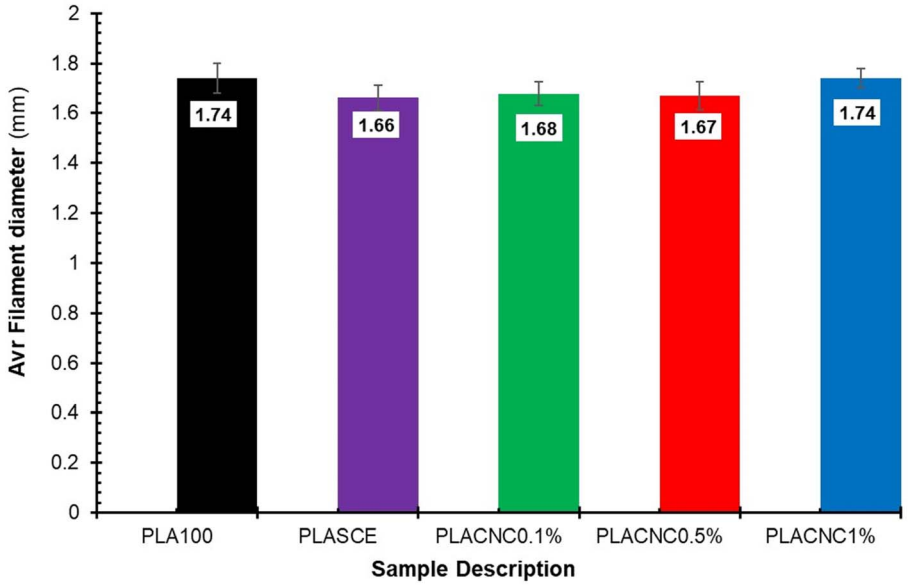

Fig. 15 The average filament diameters of the PLA and PLA/CNC bionanocomposites filaments.

the measured data. So, a Vernier calliper was used to measure filament diameters at 10 locations across a 1 meter-long filament sample. Fig. 15 shows the comparison between the average diameters of neat PLA, plasticised PLA, and bionanocomposite filament. There are no major differences between the averaged filament diameter of PLASCE (1.66 mm ± 0.05), $PLACNC_{0.1\%}$ (1.68 mm ± 0.05), and $PLACNC_{0.5\%}$ (1.67 mm ± 0.06). The average filament diameter of PLA_{100} and $PLACNC_{1\%}$ was 1.74 mm ± 0.06 and 1.74 mm ± 0.04 respectively. Most FDM 3D printers are factory calibrated to operate using a 1.75 mm filament. Using filaments with smaller or larger diameters increases the risks of inconsistent extrusion as fewer or more material gets deposited. The resulting over- or under-extrusion can severely affect the final overall dimensional and structural integrity of 3D-printed objects. In this study, the applicability of the filaments was adapted by increasing the extrusion rate of the FDM printer from 100% to 105%. This adjustment implemented on the slicing software interface of

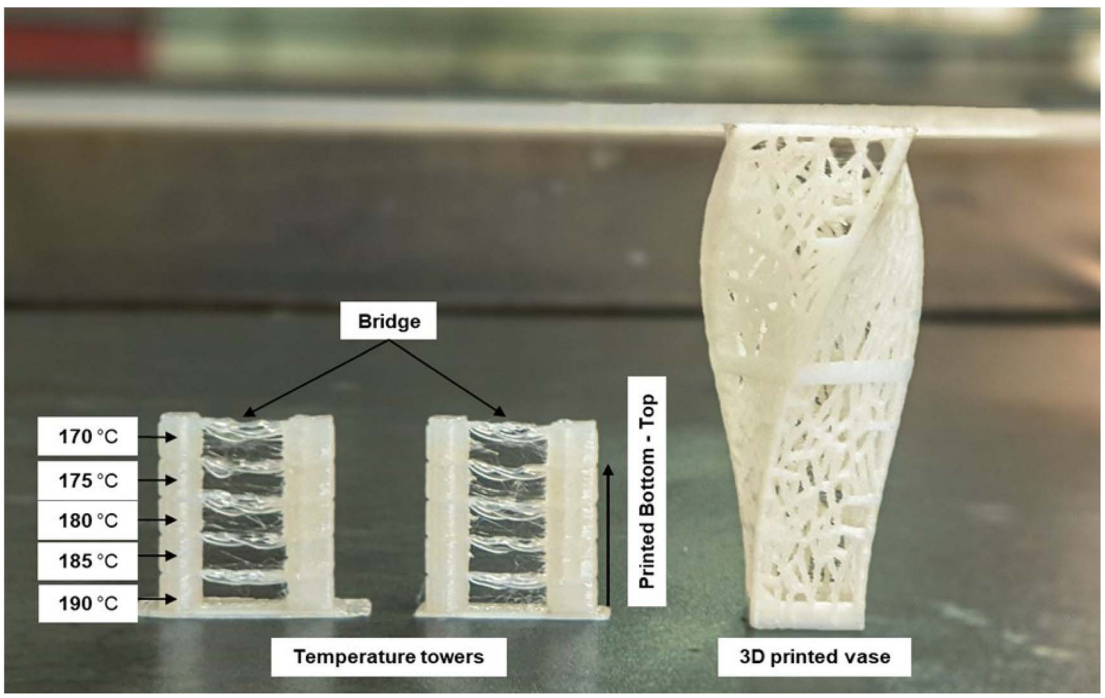

Fig. 16 FDM 3D printed temperature test tower and Voronoi tessellation vase using PLA/CNC bionanocomposite filament.

Simplify3D™ was done to compensate for the variation in the bionanocomposite filaments.

4.10. Analysis of 3D printability of PLA/CNC biocomposite filaments

The 3D printability of all the filament materials was tested on a fused deposition modelling (FDM) 3D printer. The brittle nature of the neat PLA filament (PLA_{100}) caused it to repeatedly shatter during 3D printing. However, the plasticized filament (PLASCE) and the bionanocomposite filaments did not break during 3D printing. The ability of these filaments to withstand the dynamic stresses exerted on them during the 3D printing process is attributed to successful plasticization. Furthermore, a temperature calibration step involving the 3D printing of a vertical (temperature) tower with multiple horizontal slabs (bridge) was conducted. Fig. 16 shows the temperature tower printed using $PLACNC_{0.5\%}$ (left) and PLASCE (right) filaments. The printing temperature was varied between 190–170 °C by lowering the temperature by 5 °C at the last layer of the bridge. It was observed that the quality of bridging deteriorated at lower printing temperatures. The deterioration of bridging at lower temperatures indicates that the 3D printer struggled to extrude/flow. Therefore, 190 and 185 °C appear to be the optimal 3D printing temperature for the materials. Afterwards, the $PLACNC_{0.5\%}$ filament was employed in the 3D printing of a spiral vase with Voronoi tessellation. The successful 3D printing of these parts highlights the potential use of the bionanocomposite filaments in the production of complex items.

4.11. Rheological analysis of 3D printed PLA/CNC bionanocomposites

Fig. 17a shows the plots of complex viscosity (η^*) as a function of angular frequency (ω) for plasticised PLA (PLASCE) and bionanocomposites. The incorporation of cellulose nanocrystals (CNCs) resulted in higher melt viscosity, which is attributed to reduced free volume and restricted mobility of PLA chains. $PLACNC_{1\%}$ showed the highest viscosity indicative of higher mobility inhibition of the PLA chains. However, a gradual decrease in η^* between ω = 0.1–10 rad s^{-1} for the PLASCE specimen indicates pseudoplastic (shear thinning) behaviour because of polymer chain disentanglement. Contrarily, the samples containing CNCs all exhibited constant complex viscosity (η^*) (Newtonian behaviour) within the same shear range region (ω = 0.1–10 rad s^{-1}). Nevertheless, all the specimens exhibited a sudden increase in complex viscosity (η^*) at higher angular frequencies (ω = >10 rad s^{-1}). This sudden shear thickening (dilatant) behaviour is attributed to increased PLA chain entanglement which is more prominent in PLASCE.

Meanwhile, the storage (G') and loss (G'') modulus increased with higher loading of CNCs as shown in Fig. 17b and c. The increase in G' and G'' is also attributed to the restricted mobility of PLA chains from the interactions with CNCs. The observed increase of the storage modulus (G') and low angular frequency (ω) indicates good CNCs dispersion and increased interaction with the PLA chains.[54] Fig. 17b clearly shows the effect of this

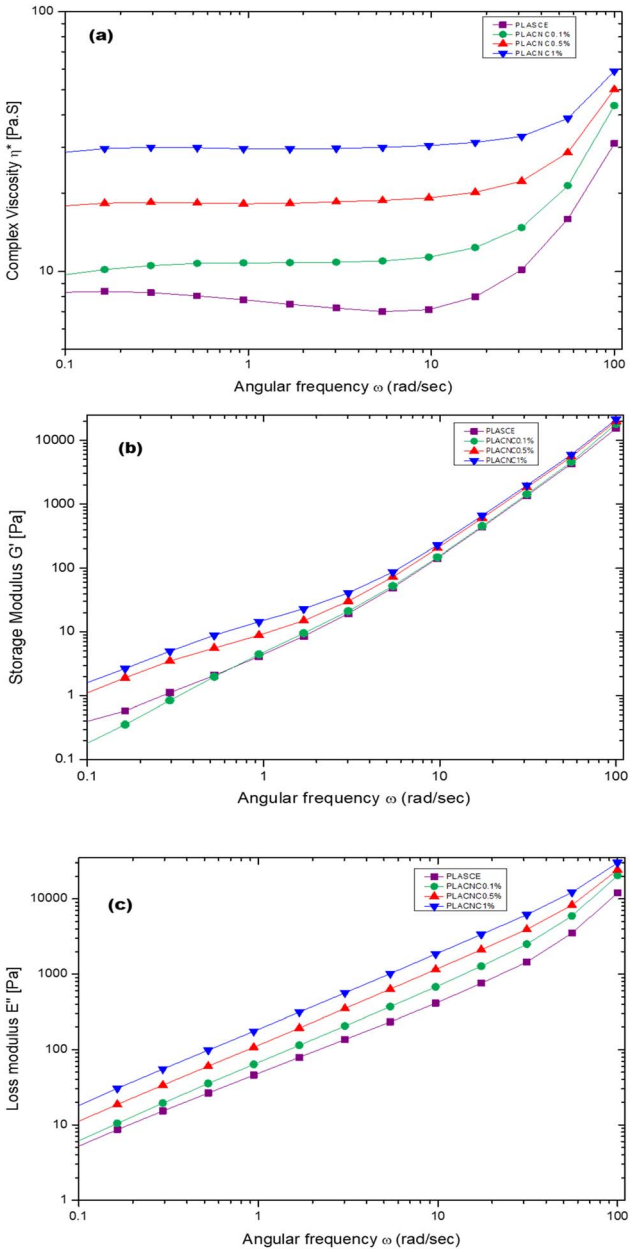

Fig. 17 Melt rheological behaviour of PLA/CNC bionanocomposites showing the evolution of; (a) complex viscosity (η^*), (b) storage (G') modulus, (c) loss (G'') modulus.

interaction on storage modulus G' was prominent in $PLACNC_{0.5\%}$ and $PLACNC_{1\%}$ specimens between ω = 0.1–5 rad s^{-1}. However, all the samples exhibited similar G' values at higher angular frequencies as the interaction between CNCs and PLA chains decayed.

5. Summary

This work demonstrated the process of fabricating PLA/CNC bionanocomposites using freeze-dried cellulose nanocrystals re-dispersed in a mixture of green solvents. The study followed the method of direct liquid feeding of re-dispersed CNCs into

the PLA melt which is a scalable process. The melt strength, viscosity and processibility of the bionanocomposites were improved by incorporating bio-based additives and food grade multifunctional chain extender. Thermal analysis of the bionanocomposites revealed improved crystallization behaviour during cooling, which resulted in the formation of mechanically and structurally stable PLA crystallites. This improvement together with the reinforcing effect of CNCs resulted in better tensile strength, tensile modulus, and flexibility of the PLA/CNC bionanocomposites filaments. The morphological analysis of the bionanocomposite filaments revealed improved filament ovality and adequate CNCs dispersion in the PLA matrix. Furthermore, the printability of the PLA/CNC bionanocomposite filaments was demonstrated using a fused deposition modelling (FDM) 3D printer. The 3D printing temperature optimization test showed that the filaments can be processed well below the thermal decomposition temperature.

Author contributions

"Conceptualization, V. C. A. and M. J. J.; methodology, V. C. A.; 3D printing, V. C. A.; formal analysis, V. C. A. and S. P. H.; investigation, V. C. A.; resources, M. J. J., S. P. H. and J. A.; data curation, V. C. A.; writing – original draft preparation, V. C. A., S. P. H. and M. J. J.; writing – review and editing, V. C. A., S. P. H. and M. J. J.; visualization, V. C. A.; supervision, M. J. J. and S. P. H.; project administration, M. J. J. and S. P. H.; funding acquisition, M. J. J., all authors have read and agreed to the published version of the manuscript.

Conflicts of interest

All the study participants provided informed consent, so there are no conflicts of interest to declare.

Acknowledgements

This research was funded by the Department of Science and Innovation (DSI), South Africa – Biorefinery Consortium Project – under the DSI Bioeconomy program, Grant number DST/CON0188/2017.

References

1 S. Kumar, V. N. Kannan and G. Sankaranarayanan, Parameter optimization of ABS-M30i parts produced by fused deposition modelling for minimum surface roughness, *Int. J. Current Eng. Technol.*, 2014, **3**, 93–97.
2 B. Coppola, N. Cappetti, L. Di Maio, P. Scarfato and L. Incarnato, 3D printing of PLA/clay nanocomposites: Influence of printing temperature on printed samples properties, *Materials*, 2018, **11**(10), 1947.
3 D. Bagheriasl, F. Safdari, P. J. Carreau, C. Dubois and B. Riedl, Development of cellulose nanocrystal-reinforced polylactide: A comparative study on different preparation methods, *Polym. Compos.*, 2019, **40**(S1), E342–E349.
4 H. Li, *et al.*, Crystallisation, mechanical properties and rheological behaviour of PLA composites reinforced by surface modified microcrystalline cellulose, *Plast., Rubber Compos.*, 2016, **45**(4), 181–187.
5 N. Herrera, A. P. Mathew and K. Oksman, Plasticized polylactic acid/cellulose nanocomposites prepared using melt-extrusion and liquid feeding: Mechanical, thermal and optical properties, *Compos. Sci. Technol.*, 2015, **106**, 149–155.
6 F. Hassouna, J.-M. Raquez, F. Addiego, V. Toniazzo, P. Dubois and D. Ruch, New development on plasticized poly (lactide): Chemical grafting of citrate on PLA by reactive extrusion, *Eur. Polym. J.*, 2012, **48**(2), 404–415.
7 D. C. França, *et al.*, Tailoring PBAT/PLA/Babassu films for suitability of agriculture mulch application, *J. Nat. Fibers*, 2019, **16**(7), 933–943.
8 Y. Lyu, Y. Chen, Z. Lin, J. Zhang and X. Shi, Manipulating phase structure of biodegradable PLA/PBAT system: Effects on dynamic rheological responses and 3D printing, *Compos. Sci. Technol.*, 2020, **200**, 108399.
9 M. J. John, N. Dyanti, T. Mokhena, V. Agbakoba and B. Sithole, Design and development of cellulosic bionanocomposites from forestry waste residues for 3d printing applications, *Materials*, 2021, **14**(13), 3462.
10 N. M. Holden, A. M. Neill, J. C. Stout, D. O'Brien and M. A. Morris, Biocircularity: a framework to define sustainable, circular bioeconomy, *Circ. Econ. Sustainability*, 2023, **3**(1), 77–91.
11 A. Hachaichi, B. Kouini, L. K. Kian, M. Asim and M. Jawaid, Extraction and characterization of microcrystalline cellulose from date palm fibres using successive chemical treatments, *J. Polym. Environ.*, 2021, **29**(6), 1990–1999.
12 L. K. Kian, M. Jawaid, H. Ariffin and Z. Karim, Isolation and characterization of nanocrystalline cellulose from roselle-derived microcrystalline cellulose, *Int. J. Biol. Macromol.*, 2018, **114**, 54–63.
13 M. Pan, X. Zhou and M. Chen, Cellulose nanowhiskers isolation and properties from acid hydrolysis combined with high-pressure homogenization, *BioResources*, 2013, **8**(1), 933–943.
14 M. N. Angles and A. Dufresne, Plasticized starch/tunicin whiskers nanocomposites. 1. Structural analysis, *Macromolecules*, 2000, **33**(22), 8344–8353.
15 M. Grunert and W. T. Winter, Nanocomposites of cellulose acetate butyrate reinforced with cellulose nanocrystals, *J. Polym. Environ.*, 2002, **10**(1), 27–30.
16 A. Mtibe, L. Z. Linganiso, A. P. Mathew, K. Oksman, M. J. John and R. D. Anandjiwala, A comparative study on properties of micro and nanopapers produced from cellulose and cellulose nanofibres, *Carbohydr. Polym.*, 2015, **118**, 1–8.
17 F. Fahma, S. Iwamoto, N. Hori, T. Iwata and A. Takemura, Effect of pre-acid-hydrolysis treatment on morphology and properties of cellulose nanowhiskers from coconut husk, *Cellulose*, 2011, **18**(2), 443–450.
18 Y. Zhang, *et al.*, Poly (lactic acid)/cellulose nanocrystal composites *via* the Pickering emulsion approach:

Rheological, thermal and mechanical properties, *Int. J. Biol. Macromol.*, 2019, **137**, 197–204.

19 K. Oksman, A. P. Mathew, D. Bondeson and I. Kvien, Manufacturing process of cellulose whiskers/polylactic acid nanocomposites, *Compos. Sci. Technol.*, 2006, **66**(15), 2776–2784.

20 E. Fortunati, *et al.*, Multifunctional bionanocomposite films of poly (lactic acid), cellulose nanocrystals and silver nanoparticles, *Carbohydr. Polym.*, 2012, **87**(2), 1596–1605.

21 S. D. Kumar, K. Venkadeshwaran and M. Aravindan, Fused deposition modelling of PLA reinforced with cellulose nano-crystals, *Mater. Today: Proc.*, 2020, **33**, 868–875.

22 D. Rigotti, A. Dorigato, A. Cataldi, L. Fambri, and A. Pegoretti, *Nanocellulose as Reinforc-Ing Agent for Biodegradable Polymers in 3D Printing Fused Deposition Modelling*, ECCM, 2018.

23 Q. Wang, *et al.*, Kinetic thermal behaviour of nanocellulose filled polylactic acid filament for fused filament fabrication 3D printing, *J. Appl. Polym. Sci.*, 2020, **137**(7), 48374.

24 N. D. Ahmad and M. W. Wildan, Preparation and properties of cellulose nanocrystals-reinforced Poly (lactic acid) composite filaments for 3D printing applications, *Results Eng.*, 2023, **17**, 100842.

25 M. Eichers, D. Bajwa, J. Shojaeiarani and S. Bajwa, Biobased plasticizer and cellulose nanocrystals improve mechanical properties of polylactic acid composites, *Ind. Crops Prod.*, 2022, **183**, 114981.

26 V. C. Agbakoba, P. Hlangothi, J. Andrew and M. J. John, Mechanical and Shape Memory Properties of 3D-Printed Cellulose Nanocrystal (CNC)-Reinforced Polylactic Acid Bionanocomposites for Potential 4D Applications, *Sustainability*, 2022, **14**(19), 12759.

27 A. N. Frone, S. Berlioz, J.-F. Chailan and D. M. Panaitescu, Morphology and thermal properties of PLA–cellulose nanofibers composites, *Carbohydr. Polym.*, 2013, **91**(1), 377–384.

28 J. Shojaeiarani, D. S. Bajwa and K. Hartman, Esterified cellulose nanocrystals as reinforcement in poly (lactic acid) nanocomposites, *Cellulose*, 2019, **26**(4), 2349–2362.

29 L. Segal, J. J. Creely, A. E. Martin and C. M. Conrad, An Empirical Method for Estimating the Degree of Crystallinity of Native Cellulose Using the X-Ray Diffractometer, *Text. Res. J.*, 1959, **29**(10), 786–794, DOI: 10.1177/004051755902901003.

30 J. I. Langford and A. Wilson, Scherrer after sixty years: a survey and some new results in the determination of crystallite size, *J. Appl. Crystallogr.*, 1978, **11**(2), 102–113.

31 L. Lin and K. Tsuchii, Dissolution behaviour of cellulose in a novel cellulose solvent, *Carbohydr. Res.*, 2022, **511**, 108490.

32 Y. Habibi, H. Chanzy and M. R. Vignon, TEMPO-mediated surface oxidation of cellulose whiskers, *Cellulose*, 2006, **13**(6), 679–687.

33 W. He, S. Jiang, Q. Zhang and M. Pan, Isolation and characterization of cellulose nanofibers from Bambusa rigida, *BioResources*, 2013, **8**(4), 5678–5689.

34 G. Tonoli, *et al.*, Properties of cellulose micro/nanofibers obtained from eucalyptus pulp fibre treated with anaerobic digestate and high shear mixing, *Cellulose*, 2016, **23**(2), 1239–1256.

35 Q. Lu, Z. Cai, F. Lin, L. Tang, S. Wang and B. Huang, Extraction of cellulose nanocrystals with a high yield of 88% by simultaneous mechanochemical activation and phosphotungstic acid hydrolysis, *ACS Sustainable Chem. Eng.*, 2016, **4**(4), 2165–2172.

36 S. Elanthikkal, U. Gopalakrishnapanicker, S. Varghese and J. T. Guthrie, Cellulose microfibres produced from banana plant wastes: Isolation and characterization, *Carbohydr. Polym.*, 2010, **80**(3), 852–859.

37 W. Chen, H. Yu, Y. Liu, P. Chen, M. Zhang and Y. Hai, Individualization of cellulose nanofibers from wood using high-intensity ultrasonication combined with chemical pretreatments, *Carbohydr. Polym.*, 2011, **83**(4), 1804–1811.

38 J.-M. Raquez, *et al.*, Surface-modification of cellulose nanowhiskers and their use as nanoreinforcers into polylactide: a sustainably-integrated approach, *Compos. Sci. Technol.*, 2012, **72**(5), 544–549.

39 D. Gaspar, *et al.*, Nanocrystalline cellulose applied simultaneously as the gate dielectric and the substrate in flexible field effect transistors, *Nanotechnology*, 2014, **25**(9), 094008.

40 I. Besbes, S. Alila and S. Boufi, Nanofibrillated cellulose from TEMPO-oxidized eucalyptus fibres: effect of the carboxyl content, *Carbohydr. Polym.*, 2011, **84**(3), 975–983.

41 K. Heritage, J. Mann and L. Roldan-Gonzalez, Crystallinity and the structure of celluloses, *J. Polym. Sci., Part A: Gen. Pap.*, 1963, **1**(2), 671–685.

42 H. Yousefi, M. Faezipour, S. Hedjazi, M. M. Mousavi, Y. Azusa and A. H. Heidari, Comparative study of paper and nanopaper properties prepared from bacterial cellulose nanofibers and fibres/ground cellulose nanofibers of canola straw, *Ind. Crops Prod.*, 2013, **43**, 732–737.

43 H. A. Silvério, W. P. F. Neto, N. O. Dantas and D. Pasquini, Extraction and characterization of cellulose nanocrystals from corncob for application as reinforcing agent in nanocomposites, *Ind. Crops Prod.*, 2013, **44**, 427–436.

44 M. Roman and W. T. Winter, Effect of sulfate groups from sulfuric acid hydrolysis on the thermal degradation behaviour of bacterial cellulose, *Biomacromolecules*, 2004, **5**(5), 1671–1677.

45 F. Beltrán, M. De La Orden, V. Lorenzo, E. Pérez, M. Cerrada and J. M. Urreaga, Water-induced structural changes in poly (lactic acid) and PLLA-clay nanocomposites, *Polymer*, 2016, **107**, 211–222.

46 M.-E. Grigora, *et al.*, Influence of reactive chain extension on the properties of 3d printed poly (Lactic acid) constructs, *Polymers*, 2021, **13**(9), 1381.

47 M. R. Ketabchi, M. Khalid, C. T. Ratnam and R. Walvekar, Mechanical and thermal properties of polylactic acid composites reinforced with cellulose nanoparticles extracted from kenaf fibre, *Mater. Res. Express*, 2016, **3**(12), 125301.

48 J.-G. Gwon, *et al.*, Mechanical and thermal properties of toluene diisocyanate-modified cellulose nanocrystal

nanocomposites using semi-crystalline poly (lactic acid) as a base matrix, *RSC Adv.*, 2016, **6**(77), 73879–73886.

49 D. Bagheriasl, P. J. Carreau, B. Riedl and C. Dubois, Enhanced properties of polylactide by incorporating cellulose nanocrystals, *Polym. Compos.*, 2018, **39**(8), 2685–2694.

50 J. Dong, C. Mei, J. Han, S. Lee and Q. Wu, 3D printed poly (lactic acid) composites with grafted cellulose nanofibers: Effect of nanofiber and post-fabrication annealing treatment on composite flexural properties, *Addit. Manuf.*, 2019, **28**, 621–628.

51 N. Najafi, M. Heuzey, P. Carreau and P. M. Wood-Adams, Control of thermal degradation of polylactide (PLA)-clay nanocomposites using chain extenders, *Polym. Degrad. Stab.*, 2012, **97**(4), 554–565.

52 Q. Meng, M.-C. Heuzey and P. J. Carreau, Control of thermal degradation of polylactide/clay nanocomposites during melt processing by chain extension reaction, *Polym. Degrad. Stab.*, 2012, **97**(10), 2010–2020.

53 N. Ljungberg and B. Wesslen, The effects of plasticizers on the dynamic mechanical and thermal properties of poly (lactic acid), *J. Appl. Polym. Sci.*, 2002, **86**(5), 1227–1234.

54 F. Wu, *et al.*, Interfacial relaxation mechanisms in polymer nanocomposites through the rheological study on polymer/grafted nanoparticles, *Polymer*, 2016, **90**, 264–275.